J. Fluid Mech. (2005), *vol.* 527, *pp.* 353–377. © 2005 Cambridge University Press
DOI: 10.1017/S0022112004002800 Printed in the United Kingdom

Instability in flow through elastic conduits and volcanic tremor

By NEIL J. BALMFORTH[1,2], R. V. CRASTER[3] AND A. C. RUST[2]

[1]Department of Mathematics, University of British Columbia, 1984 Mathematics Road, Vancouver, BC, V6T 1Z2, Canada

[2]Department of Earth & Ocean Sciences, University of British Columbia, 6339 Stores Road, Vancouver, BC, V6T 1Z4, Canada

[3]Department of Mathematics, Imperial College, London SW7 2BZ, UK

(Received 17 March 2004 and in revised form 2 October 2004)

The stability of fluid flow through a narrow conduit with elastic walls is explored, treating the fluid as incompressible and viscous, and the walls as semi-infinite linear Hookean solids. Instabilities analogous to roll waves occur in this system; we map out the physical regime in which they are excited. For elastic wave speeds much higher than the fluid speed, a critical Reynolds number is required for instability. However, that critical value depends linearly on wavenumber, and so can be made arbitrarily small for long waves. For smaller elastic wave speeds, the critical Reynolds number is reduced still further, and Rayleigh waves can be destabilized by the fluid even at zero Reynolds number. A brief discussion is given of the nonlinear dynamics of the instabilities for large elastic wave speed, and the significance of the results to the phenomenon of volcanic tremor is presented. Although magma itself seems unlikely to generate flow-induced vibrations, the rapid flow through fractured rock of low-viscosity fluids exsolved from magma appears to be a viable mechanism for volcanic tremor.

1. Introduction

Sustained ground vibrations are observed at most active volcanoes, and are sometimes a precursor to eruptions. This 'volcanic tremor' is often found to be distinctly harmonic, and analysis of time series reveals fairly well-defined spectral peaks at periods of seconds (e.g. Julian 1994; Hagerty *et al.* 2000). The phenomenon is thought to be associated with the subsurface unsteady flow of magma, although the nature and origin of the fluid motions has not yet been determined (Konstantinou & Schlindwein 2002). One theoretical model proposed by Julian (1994) advances the premise that tremor arises from instability in magma conduits owing to interaction between the flowing magma and the surrounding rock. This instability is analogous to that seeding the roll waves which travel on thin falling fluid films and propagate down turbulent water courses (e.g. Chang 1994), and related explanations have been advocated for unsteady blood flow and 'Korotkov sounds' in physiology (Pedley 1980; Brook, Pedley & Falle 1999).

The destabilization of fluid flow by a compliant wall is a familiar notion in several other branches of fluid mechanics, notably in drag reduction in engineering (Benjamin 1960, 1963; Landahl 1962) and in air flow through passages in the lung (LaRose & Grotberg 1997; Moriarty & Grotberg 1999). In these contexts, the flow is relatively high speed (high Reynolds number), and the compliant walls typically take the form

https://doi.org/10.1017/S0022112004002800 Published online by Cambridge University Press

of thin tubes or layers. Consequently, much work has gone into understanding the instability of inviscid or potential flow, and the theory of elastic shells or plates is used to provide boundary conditions at the compliant walls. Instabilities are usually found to arise for flow speeds greater than the natural elastic wave speeds of the wall (Gad-El-Hak, Blackwelder & Riley 1984; Duncan, Waxman & Tulin 1985). By contrast, in the volcanic problem, the underlying flow of magma is much slower (low Reynolds number), and certainly rather less than the elastic wave speeds in the surrounding rock. Moreover, the geometry of the volcanic conduit is quite different because the rock occupies a far larger region than the conduit itself. Overall, these differences force us into a separate theoretical discussion of volcanic tremor. A notable exception is the approach taken in the series of papers by Kumaran and collaborators, which bears some similarity to the route followed in the current paper (Kumaran, Fredricksen & Pinkus 1994; Srivatsan & Kumaran 1997; Shankar & Kumaran 2002).

In this regard, although Julian's model shows that flow instability is a possible mechanism for tremor, it is based on phenomenological arguments and not derived from the governing equations. That system should consist of fluid equations for the magma and the equations of elasticity for the surrounding solid rock. Consequently, a more quantitative model of volcanic tremor is still desired in order to assess more completely whether the flow instability mechanism truly lies at the heart of the phenomenon. Furthermore, a better theoretical model of the phenomena might prove useful as a tool to aid the prediction of eruptions and other dangerous volcanic events.

The purpose of the present paper is to take the mathematical modelling of Julian's mechanism a step further. In § 2, we analyse the governing equations for an idealized volcanic conduit. In particular, in §§ 3 and 4, we consider viscous flow along a long uniform conduit sandwiched between two semi-infinite elastic slabs, and study the excitation of propagating waves, using long-wave expansion and linear stability theory. This approach parallels theory presented for roll waves in other contexts (Brook, Pedley & Falle 1999; Balmforth & Mandre 2004; Balmforth & Liu 2004). We also briefly describe results for nonlinear waves, uncovering what appears to be complicated spatio-temporal dynamics (§ 5). Overall, the results confirm that Julian's mechanism is plausible, although the physical conditions required for instability seem somewhat removed from those expected geologically. We offer some remarks placing the mathematical model into the context of volcanic tremor in our conclusions (§ 6), and mention the main direction of future work.

2. Formulation of the model

Our idealization of the physical problem is shown schematically in figure 1. We consider a conduit, or slot, described by a Cartesian coordinate system in which x points along the slot and y is perpendicular to it. The magma, contained in $-h(x,t) < y < h(x,t)$, is treated as a Newtonian viscous fluid, and the surrounding rock as an elastic solid. The slot is relatively narrow, being a crack that is opened by an ambient fluid pressure comparable to the stresses within the rock. The crack supports a flow driven by a pressure gradient corresponding to a pressure difference that could be rather smaller than the ambient pressure. We take the crack to be symmetric about $y = 0$, and therefore consider only varicose disturbances.

2.1. *The fluid*

The fluid is described by an Eulerian coordinate system, (x, y), together with the velocity field, $(u(x,y,t), v(x,y,t))$, and pressure, $p(x,y,t)$. The governing equations

https://doi.org/10.1017/S0022112004002800 Published online by Cambridge University Press

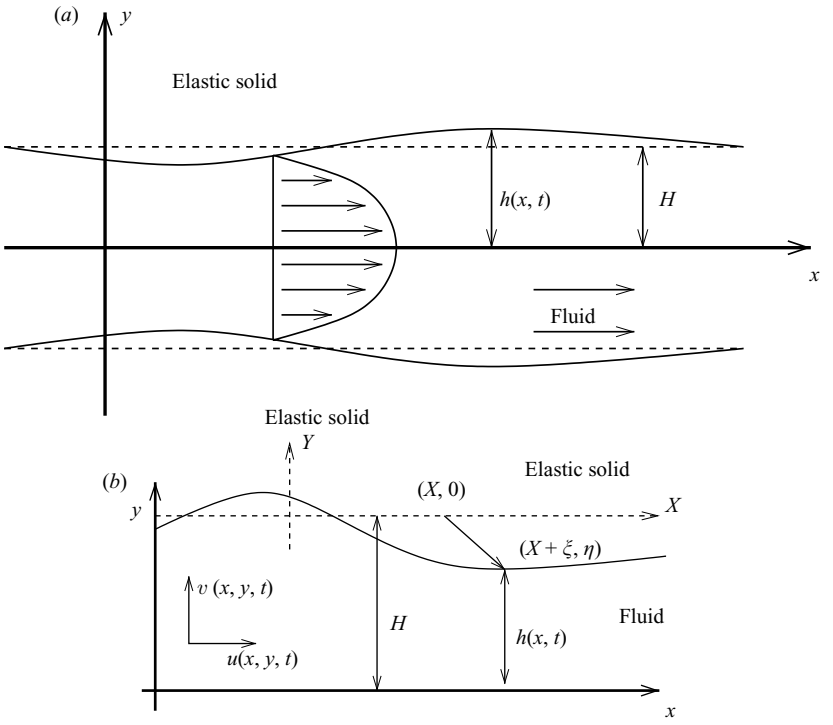


FIGURE 1. Idealization of the magma conduit. (*a*) The geometry of a fluid moving through a conduit bounded by semi-infinite elastic solids. (*b*) The coordinate systems used to describe the fluid and solid.

are given by conservation of momentum,

$$\rho(u_t + uu_x + vu_y) = -p_x + \rho\nu(u_{xx} + u_{yy}), \tag{2.1}$$

$$\rho(v_t + uv_x + vv_y) = -p_y + \rho\nu(v_{xx} + v_{yy}) \tag{2.2}$$

and continuity,

$$u_x + v_y = 0, \tag{2.3}$$

where ρ and ν are the fluid density and viscosity, respectively. The fluid stresses are given by the tensor,

$$\begin{pmatrix} 2\rho\nu u_x - p & \rho\nu(u_y + v_x) \\ \rho\nu(u_y + v_x) & 2\rho\nu v_y - p \end{pmatrix}. \tag{2.4}$$

2.2. *The elastic solid*

The elastic solid is described by a coordinate system, (X, Y), based on the unstressed solid arrangement: under the imposed ambient and dynamic stresses, an elastic element is displaced from the position (X, Y) to $(X + \xi, Y + \eta)$, where the displacement field, $(\xi(X, Y, t), \eta(X, Y, t))$, satisfies the equations of motion,

$$\rho_s \xi_{tt} = \frac{\partial \sigma_{XX}}{\partial X} + \frac{\partial \sigma_{XY}}{\partial Y}, \qquad \rho_s \eta_{tt} = \frac{\partial \sigma_{XY}}{\partial X} + \frac{\partial \sigma_{YY}}{\partial Y}, \tag{2.5}$$

where ρ_s is the solid density and σ_{IJ} denote the components of the elastic stress.

https://doi.org/10.1017/S0022112004002800 Published online by Cambridge University Press

We take the elastic stress–strain relation to be linear, isotropic and Hookean:

$$\{\sigma_{IJ}\} = \begin{pmatrix} (2\mu+\lambda)\xi_X + \lambda\eta_Y & \mu(\xi_Y+\eta_X) \\ \mu(\eta_X+\xi_Y) & (2\mu+\lambda)\eta_Y + \lambda\xi_X \end{pmatrix}, \tag{2.6}$$

where λ and μ represent Lamé constants, which are related to Poisson's ratio, ϖ, via $\varpi = \lambda/(2(\mu+\lambda))$.

In the volcanic setting, the fluid speeds are far less than the speeds at which elastic waves propagate in the solid (typically the latter are $O(10^3)\,\mathrm{m\,s^{-1}}$). In this situation, we could drop the acceleration terms from (2.5) so the elastic medium is quasi-static. We give a general discussion of the linear stability of waves propagating in the fluid without making this further simplification, but when considering nonlinear waves we resort to the quasi-static approximation. Our motivation for the more general treatment of the linear stability problem is partly to present a coherent mathematical analysis. However, elastic wave speeds in viscoelastic coatings, polymer gels and biological tissues can be relatively small (as low as centimetres per second – Gad-El-Hak *et al.* 1984; Moriarty & Grotberg 1999; Muralikrishnan & Kumaran 2002), highlighting the relevance to other physical problems. In this limit, we also make contact with the existing results for high-speed flows.

2.3. *Boundary conditions*

Symmetry at the centreline demands that $u_y = v = 0$ on $y = 0$. On the channel walls, there is no slip and so the displacement of the wall and its rate of change must match with the corresponding fluid displacement and velocities, i.e.

$$x = X + \xi(X,0,t), \qquad h(x,t) = H + \eta(X,0,t), \tag{2.7}$$

$$u(x,h,t) = \xi_t(X,0,t), \qquad v(x,h,t) = \eta_t(X,0,t). \tag{2.8}$$

Stress balance forces us to make the tangential and normal stresses continuous, which in the absence of any interfacial tension requires that

$$\frac{1}{1+h_x^2}\begin{pmatrix} 1 & h_x \\ -h_x & 1 \end{pmatrix}\begin{pmatrix} 2\rho\nu u_x - p & \rho\nu(u_y+v_x) \\ \rho\nu(u_y+v_x) & 2\rho\nu v_y - p \end{pmatrix}\begin{pmatrix} -h_x \\ 1 \end{pmatrix} = \begin{pmatrix} \sigma_{XY} \\ \sigma_{YY} \end{pmatrix}, \tag{2.9}$$

on $y = h$ or $Y = 0$. Since the wall is a material surface, we have the kinematic condition,

$$h_t + u(x,h,t)h_x = v(x,h,t). \tag{2.10}$$

The remaining conditions to be specified include the far-field boundary conditions within the elastic solid and the conditions arising at the edges of the crack should it be finite. For the former, we demand that disturbances either decay for $Y \to \pm\infty$, or correspond to purely outgoing waves. We avoid discussion of the edge conditions in the current paper and adopt periodic boundary conditions in x and X.

2.4. *Non-dimensionalization*

We remove dimensions from the governing equations as follows. We define H as a characteristic half-thickness of the channel and measure lengths along the slot with the unit, L. We scale velocities (u, v) with the characteristic speeds, U and UH/L, and time t with L/U:

$$x = L\tilde{x}, \quad z = H\tilde{z}, \quad u = U\tilde{u}, \quad v = UH\tilde{v}/L, \quad t = L\tilde{t}/U, \tag{2.11}$$

where the tilde indicates dimensionless variables. The aspect ratio $\epsilon = H/L$ is assumed small and we shall take advantage of this below to simplify the equations. We also take $p = (\rho\nu UL/H^2)\tilde{p}$ to balance axial pressure gradient with shear stress.

https://doi.org/10.1017/S0022112004002800 Published online by Cambridge University Press

On dropping the tilde decoration, the dimensionless fluid equations become

$$R(u_t + uu_x + vu_y) = -p_x + u_{yy} + \epsilon^2 u_{xx}, \tag{2.12}$$

$$\epsilon^2 R(v_t + uv_x + vv_y) = -p_y + \epsilon^2(v_{yy} + \epsilon^2 v_{xx}), \tag{2.13}$$

and

$$u_x + v_y = 0, \tag{2.14}$$

with a scaled Reynolds number parameter, $R = \epsilon U H/\nu$, assumed order one.

For the elastic solid, we adopt $(\xi, \eta) = H(\tilde{\xi}, \tilde{\eta})$ and $(X, Y) = L(\tilde{X}, \tilde{Y})$. We also define the potentials, $\xi = \phi_X + \chi_Y$ and $\eta = \phi_Y - \chi_X$, which, after dropping the tildes, reduce the equations of motion to the two wave equations,

$$\phi_{tt} = \alpha^2(\phi_{XX} + \phi_{YY}), \qquad \chi_{tt} = \beta^2(\chi_{XX} + \chi_{YY}), \tag{2.15}$$

where α and β are the dimensionless compressional and shear elastic wave speeds (inverse Mach numbers):

$$\alpha^2 = \frac{\lambda + 2\mu}{\rho_s U^2}, \qquad \beta^2 = \frac{\mu}{\rho_s U^2}. \tag{2.16}$$

The compressional wave speed is always greater than the shear wave speed ($\alpha > \beta$).

The match of stresses and displacements at the wall gives

$$x = X + \epsilon\xi(X, 0, t), \qquad h - 1 = \eta(X, 0, t), \tag{2.17}$$

$$u(x, h, t) = \epsilon\xi_t(X, 0, t), \qquad v(x, h, t) = \eta_t(X, 0, t), \tag{2.18}$$

$$(G\sigma_{YY} + p)\big(1 + \epsilon^2 h_x^2\big) = -2\epsilon^2\big[u_x\big(1 - \epsilon^2 h_x^2\big) + h_x(u_y + \epsilon^2 v_x)\big], \tag{2.19}$$

$$G\sigma_{XY}\big(1 + \epsilon^2 h_x^2\big) = \epsilon(u_y + \epsilon^2 v_x)\big(1 - \epsilon^2 h_x^2\big) - 4\epsilon^3 h_x u_x, \tag{2.20}$$

where

$$G = \frac{\epsilon^2 H\mu}{\rho\nu U} \tag{2.21}$$

is a stiffness parameter and we have non-dimensionalized the stresses by the unit, $\mu H/L$.

3. Propagating waves along a long crack

3.1. *The equilibrium fiddle*

Our idealization envisages the conduit as being held open by sustained ambient pressure that is supplemented by a weaker pressure gradient along the slot which drives the flow. A complicating aspect of this idealization is that the pressure gradient exerts a differential stress on the elastic wall, inducing a deformation which will not necessarily be uniform. Consequently, the conduit may taper or widen with distance. Below, we aim to study waves propagating along the conduit, and any non-uniformity complicates the description. For the sake of simplicity, we make a first approximation in which we ignore any x-dependent deformation of the elastic walls and assume that the equilibrium conduit is of uniform thickness, but retain the pressure gradient to drive a mean flow. In general, this is an approximation similar to the edifice used in physiological contexts (e.g. Brook *et al.* 1999).

With the approximation, the undisturbed conduit can be taken to have a semi-thickness of $h = 1$, and we further set

$$p_x \longrightarrow -3, \qquad u \longrightarrow U(y) = \tfrac{3}{2}(1 - y^2), \tag{3.1}$$

to arrive at an equilibrium flow solution with unit flux through $y \geqslant 0$.

https://doi.org/10.1017/S0022112004002800 Published online by Cambridge University Press

3.2. *Boundary-layer model*

To leading order in ϵ, the fluid equations reduce to the 'boundary-layer model',

$$R(u_t + uu_x + vu_y) = -p_x + u_{yy}, \tag{3.2}$$

$$p_y = 0 \quad \text{or} \quad p = p(x,t), \qquad u_x + v_y = 0 \tag{3.3}$$

(cf. Chang, Demekhin & Kopelevich 1993). The solution must be matched with that for the elastic solid at the compliant wall: to leading order in ϵ, the match is

$$x = X, \quad h - 1 = \eta, \quad u = 0, \quad v = \eta_t, \quad p = -G\sigma_{YY}, \quad \sigma_{XY} = 0. \tag{3.4}$$

Assuming an infinite domain in X, we may solve the equations for the elastic solid using Fourier transforms in space and time. After some algebra, we arrive at the relation,

$$p = G\int_{-\infty}^{\infty}\int_{-\infty}^{\infty} D(k, \mathrm{i}\omega)\hat{h}(k,\omega)\mathrm{e}^{\mathrm{i}kx+\mathrm{i}\omega t}\,\mathrm{d}k\,\mathrm{d}\omega, \tag{3.5}$$

where $\hat{h}(k,\omega)$ is the double Fourier transform of $h(x,t)-1$,

$$D(k,\Lambda) = -\frac{\beta^2}{\Lambda^2\kappa_\alpha}\left[4k^2\kappa_\alpha\kappa_\beta - \left(\frac{\Lambda^2}{\beta^2}+2k^2\right)^2\right], \tag{3.6}$$

$$\kappa_\alpha^2 = k^2 - \omega^2/\alpha^2, \qquad \kappa_\beta^2 = k^2 - \omega^2/\beta^2, \tag{3.7}$$

and we take $\mathrm{Re}(\kappa_j) > 0$, $j = \alpha$ or β, should those real parts be finite, or $\mathrm{Im}(\kappa_j) > 0$ if the exponent is purely imaginary (signifying an outgoing wave). For a periodic, but finite, conduit we may perform the same reduction, but with a discrete Fourier transform in x. Either way, (3.5) proves useful for linear stability theory.

Note that, if $\omega \ll \beta k$, (3.6) reduces further:

$$D(k,\Lambda) \to 2|k|\left(1-\frac{\beta^2}{\alpha^2}\right) = 2|k|\frac{\mu+\lambda}{2\mu+\lambda} = \frac{|k|}{1-\varpi}. \tag{3.8}$$

The double Fourier transform then reduces to a spatial Hilbert transform, which is a standard result for static elasticity problems (e.g. England 1971; Muskhelishvili 1953).

3.3. *Slot-averaging*

At zero Reynolds number, $R = 0$, the fluid system in (3.2) can be integrated to find the flow profile, $u = -p_x(h^2 - y^2)/2$. This further sets the stage for a lubrication-type analysis of the problem. However, as we see later, there is no instability in this limit of the problem, at least for large elastic wave speeds, so there seems little point in proceeding down this avenue. However, the reduction of the flow profile suggests a further approximation based on averaging the equations across the slot, but retaining inertia. This approach is equivalent to the classical use of von Kármán–Pohlhausen power integrals in boundary-layer theory and is much used for falling fluid films and streams (Chang 1994), where it leads to models that predict the growth of roll waves beyond a threshold in Reynolds number. We integrate (3.2) and continuity across the slot and adopt the ansatz,

$$u(x,y,t) = \tfrac{3}{2}U(x,t)\left(1-\frac{y^2}{h^2}\right), \tag{3.9}$$

https://doi.org/10.1017/S0022112004002800 Published online by Cambridge University Press

where $U(x,t)$ is not yet known, to compute the integrals of u. This leads to two coupled evolution equations for U and h:

$$R\left[(hU)_t + \tfrac{6}{5}(U^2h)_x\right] = -hp_x - \frac{3U}{h}, \qquad h_t + (Uh)_x = 0. \tag{3.10}$$

The pressure gradient in (3.10) is determined from matching with the elastic solid, and specifically (3.5).

The slot-averaged model in (3.10) is useful for further analysis, but shares a defect in common with similar approaches for fluid films, namely that it incorrectly predicts the critical Reynolds number for the onset of instability. An improvement over (3.10) can be found by introducing a higher-order polynomial for the flow profile (Ruyer-Quil & Manneville 2000):

$$u(x,y,t) = \sum_{j=0}^{4} a_j(x,t)\left[\left(1-\frac{y}{h}\right)^{j+1} - \left(\frac{j+1}{j+2}\right)\left(1-\frac{y}{h}\right)^{j+2}\right]. \tag{3.11}$$

The aim of the improvement is to correct the critical Reynolds number by suitably selecting the amplitudes, $a_j(x,t)$, which leads to the alternative, slot-averaged model,

$$R\left(q_t + \frac{17q}{7h}q_x - \frac{9q^2}{7h^2}h_x\right) = -\frac{5}{6}hp_x - \frac{5q}{2h^2}, \qquad h_t + q_x = 0, \tag{3.12}$$

where the flux, $q = \int_0^h u\,\mathrm{d}y$, now appears as a dynamical variable. As shown below, (3.12) correctly predicts the onset of long-wave instability. Below, we refer to the system (3.10) as the 'simplest' slot-averaged model, and (3.12) as the 'improved' version.

4. Linear stability theory

We perform a linear stability analysis of the boundary-layer model by introducing the decomposition,

$$u = U + \psi_y(y)\,\mathrm{e}^{\mathrm{i}kx+\Lambda t},\ v = -\mathrm{i}k\psi(y)\,\mathrm{e}^{\mathrm{i}kx+\Lambda t},\ h = 1+\hat{h}\,\mathrm{e}^{\mathrm{i}kx+\Lambda t},\ p = \hat{p}\,\mathrm{e}^{\mathrm{i}kx+\Lambda t}, \tag{4.1}$$

where k is the wavenumber and Λ the complex growth rate, and then linearizing in the amplitudes, $\hat{h}$ etc. Once the equations are linearized, the solution can be normalized such that $\hat{h}\to 1$. The linearized version of (3.2) is

$$\psi''' = \mathrm{i}k\hat{p} + R[(\Lambda + \mathrm{i}kU)\psi' - \mathrm{i}kU'\psi], \tag{4.2}$$

and the boundary conditions are $\psi(0) = \psi''(0) = 0$,

$$U'(1) + \psi'(1) = \Lambda + \mathrm{i}k\psi(1) = 0, \qquad \hat{p} = GD(k,\Lambda), \tag{4.3}$$

where $D(k,\Lambda)$, is defined in (3.6).

In terms of wave speed, $c \equiv \mathrm{i}\Lambda/k$, the linear equations become

$$\psi''' = \mathrm{i}kG\left\{D + \frac{R}{G}[(U-c)\psi' - U'\psi]\right\}, \qquad U'(1) + \psi'(1) = \psi(1) - c = 0, \tag{4.4}$$

which illustrate how a change of G corresponds to a rescaling of k and R. Moreover, we anticipate that the main parameter governing stability is $R/G = \rho U^2/\epsilon\mu \equiv \rho/\rho_s\epsilon\beta^2$.

https://doi.org/10.1017/S0022112004002800 Published online by Cambridge University Press

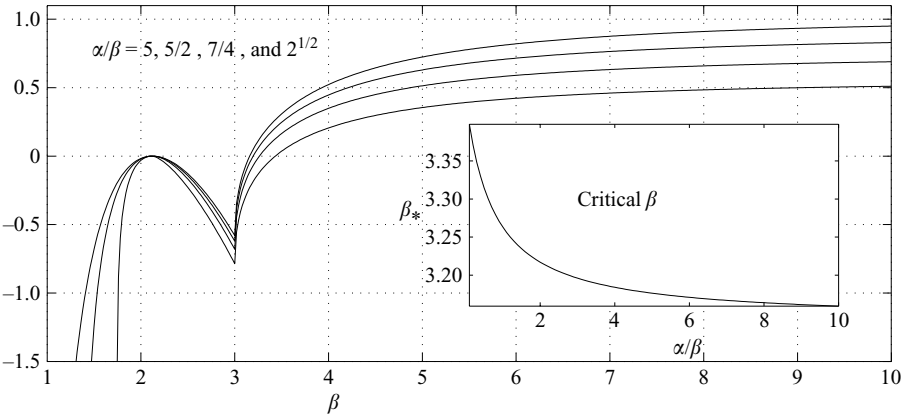


FIGURE 2. Scaled 'elastic' contribution to growth rate against β for four values of α/β (this contribution must be scaled by G). The inset shows the critical value of β for which the contribution changes sign. This condition corresponds to the Rayleigh wave speed equalling the propagation speed of fluid disturbances (three).

4.1. *Long waves*

We solve the linear boundary-layer model via a long-wave expansion of the form,

$$\psi = \psi_0 + k^2\psi_2 + \cdots, \quad \hat{p} = k\hat{p}_1 + \cdots, \quad \Lambda = k\Lambda_1 + k^3\Lambda_3 + \cdots, \quad R = kR_1. \tag{4.5}$$

The exercise is standard, and furnishes the solution,

$$\Lambda_1 = -3\mathrm{i}, \qquad \Lambda_3 = \tfrac{6}{5}R_1 - \frac{G\alpha\beta^2}{27\sqrt{\alpha^2-9}}\left[\frac{4}{\alpha\beta}\sqrt{(\alpha^2-9)(\beta^2-9)} - \left(\frac{9}{\beta^2}-2\right)^2\right]. \tag{4.6}$$

Thus, inertia is destabilizing, and the flow is unstable to long waves provided $R > R_c$, where

$$R_c = \frac{5kG\alpha\beta^2}{162\sqrt{\alpha^2-9}}\left[\frac{4}{\alpha\beta}\sqrt{(\alpha^2-9)(\beta^2-9)} - \left(\frac{9}{\beta^2}-2\right)^2\right]. \tag{4.7}$$

This threshold can be made arbitrarily small by selecting waves of increasingly long wavelength. If $\beta \to \infty$ with α/β held fixed, $R_c \to 5kG(1-\beta^2/\alpha^2)/9$.

A key feature of (4.6) is that the second term, which arises from the deformation of the elastic wall, is stabilizing for large elastic wave speeds. However, as those wave speeds decrease, the sign of this term switches (see figure 2), and the deformation of the wall also becomes destabilizing, implying that there is no threshold in Reynolds number for long-wave instability. The conduit is then unstable even in the lubrication limit. The critical elastic wave speed β is also shown in figure 2. The switch occurs when an elastic wave speed approaches the speed with which disturbances propagate naturally in the fluid (equal to three with the current non-dimensionalization). More specifically, the switch is at a Rayleigh wave speed of three, as described further in § 4.4. This result is of the same flavour as that reported by Kumaran *et al.* (1994) for flow down a gel-walled tube.

4.2. *Short (or nearly inviscid) waves*

We derive short-wavelength estimates for the eigenvalue Λ of the boundary-layer model as follows (cf. Chang *et al.* 1993). For $k \gg 1$ or $R \gg 1$, over the bulk of the

https://doi.org/10.1017/S0022112004002800 Published online by Cambridge University Press

fluid the term ψ''' in (4.2) is negligible, in which case,

$$(U-c)^2\frac{\mathrm{d}}{\mathrm{d}y}\left(\frac{\psi}{U-c}\right)=-\frac{GD(k,\Lambda)}{R}, \tag{4.8}$$

where $c=-\mathrm{i}\Lambda/k$ is the complex wave speed. We readily integrate:

$$\psi=-\frac{GD}{R}(U-c)\int_0^y\frac{\mathrm{d}\tilde{y}}{[U(\tilde{y})-c]^2}\equiv\psi_I, \tag{4.9}$$

on imposing $\psi(0)=\psi''(0)=0$. This solution cannot be made to satisfy the remaining boundary conditions, reflecting how a viscous sublayer arises near the wall. There, we must reinstate ψ''', to find the solution, $\psi=\psi_I+\psi_B$, with

$$\psi_B\sim B\mathrm{e}^{-\varsigma(1-y)},\qquad \varsigma=(1-\mathrm{i})\sqrt{\frac{kcR}{2}}, \tag{4.10}$$

where B is a constant of integration. Enforcing the boundary conditions (bearing in mind that $cR\psi_I'=\hat{p}+3R\psi_I$ and $\psi_B'=\varsigma B$ at $y=1$) now provides the dispersion relation,

$$cR=GD\left[\frac{1}{3-\varsigma c}+c\int_0^1\frac{\mathrm{d}y}{(U-c)^2}\right] \tag{4.11}$$

$$cR=\frac{GD}{3-c\varsigma}+\frac{GD}{2c-3}\left[1+\frac{2c}{\sqrt{3(2c-3)}}\tan^{-1}\sqrt{\frac{3}{2c-3}}\right]. \tag{4.12}$$

Note that the inviscid problem corresponds to taking the limit $|\varsigma|\to\infty$ with G/R fixed in the formulae above and dropping ψ_B, in which case (4.12) is exact. Notably, in the inviscid limit, we can have $c\to 3/2$ for the neutrally stable case and a critical layer develops which we briefly discuss in § 4.4.

The dispersion relation (4.12) can be simplified further given that $k\gg 1$, although the precise details depend upon the size of the elastic wave speeds. We present some of the details in Appendix A, and summarize the main results as follows. Let $c_r=\mathrm{Re}(c)$ and $\Lambda_r=\mathrm{Re}(\Lambda)$. Then, for $c_r\ll\beta$,

$$c_r\sim\sqrt{\frac{2kG}{R}\left(1-\frac{\beta^2}{\alpha^2}\right)},\qquad \Lambda_r\sim-k^{3/4}. \tag{4.13}$$

Alternatively, for $c_r\sim\beta$, the eigenvalues satisfy at leading order

$$D_R(c_r)=D(k,-ikc_r)=0. \tag{4.14}$$

This is the dispersion relation for an elastic half-space bounded by an shear-free interface at fixed pressure. Consequently, the solutions are Rayleigh waves (Love 1944) with $c_r=c_R$. The Rayleigh waves occur as counter-propagating pairs (the symmetry-breaking due to the direction of fluid flow does not appear at leading order). The Rayleigh waves propagating backwards with respect to the fluid appear to be always relatively strongly damped, and we ignore them henceforth. At higher-order, the forward-propagating Rayleigh waves become modified by viscous dissipation in the fluid, and $\Lambda_r\sim-k^{-1/2}$.

These results imply that when the elastic wave speeds are large, there are two scaling regimes (at fixed Reynolds number). First, for $1\ll k^{1/2}\ll\alpha,\beta$, the growth rate plummets as $-k^{3/4}$ (and the propagation speed increases as $k^{1/2}$). When $k^{1/2}\sim\alpha,\beta$,

https://doi.org/10.1017/S0022112004002800 Published online by Cambridge University Press

however, the disturbances become Rayleigh-like waves and the growth rate turns around and approaches zero from below as $-k^{-1/2}$. Overall, short waves are stable.

4.3. *Slot-averaged theory*

The simplest theory (3.10) predicts the dispersion relation,

$$9-\frac{3\mathrm{i}\Lambda}{k}+\mathrm{i}R\left(\frac{-12\mathrm{i}\Lambda}{5}+\frac{6k}{5}-\frac{\Lambda^2}{k}\right)=\mathrm{i}kGD(k,\Lambda). \tag{4.15}$$

The second, improved, theory (3.12) gives

$$9-\frac{3\mathrm{i}\Lambda}{k}+\mathrm{i}R\left(\frac{54k}{35}-\frac{102\mathrm{i}\Lambda}{35}-\frac{6\Lambda^2}{5k}\right)=\mathrm{i}kGD(k,\Lambda). \tag{4.16}$$

We analyse the second of these for comparison with the earlier results. Marginal stability occurs for $\Lambda=\mathrm{i}\omega$, with ω real. Thence, provided κ_α and κ_β remain real,

$$\omega=-3k,\qquad R=\frac{5kG\alpha\beta^2}{162\sqrt{\alpha^2-9}}\left[\frac{4}{\alpha\beta}\sqrt{(\alpha^2-9)(\beta^2-9)}-\left(\frac{9}{\beta^2}-2\right)^2\right]. \tag{4.17}$$

This is identical to the long-wave results of the boundary-layer model (though it is not restricted to long waves). A similar calculation for the first slot-averaged model gives a result in error by a factor of order unity, vindicating our improvement of that theory.

For an infinite elastic wave speed, short waves have the limiting eigenvalues,

$$\mathrm{Re}(\Lambda)\sim-\frac{5}{4R},\qquad \mathrm{Im}(\Lambda)\sim-k^{3/2}\sqrt{\frac{5G}{3R}\left(1-\frac{\beta^2}{\alpha^2}\right)}, \tag{4.18}$$

and are therefore always stable. For finite α and β, on the other hand, short waves once again limit to Rayleigh waves with wave speed, c_R. The damping or growth of these modes appears at order k^{-2}, leading to

$$\mathrm{Re}(\Lambda)\sim\frac{3(c_R-3)}{kGD_R'(c_R)}, \tag{4.19}$$

where $D_R(c_r)\equiv D(k,-\mathrm{i}kc_R)/k$. As long as $k^{1/2}\ll\alpha,\beta$, the growth rate therefore first decreases and flattens out to a minimum value near $-5/4R$. Once $k^{1/2}\sim\alpha,\beta$, the growth rate begins to increase back toward zero. Because $D_R'(c_R)<0$, the short waves are only stable if $c_R>3$. That is, if the Rayleigh waves are slower than fluid disturbances, they are destabilized by the coupling with the fluid; faster waves are stable. These trends are illustrated below, and have some similarities with the results of the boundary-layer theory described earlier.

4.4. *Numerical results*

We summarize and extend the results above using numerical computations with the linear boundary-layer model, as shown in figures 3–5. We take $G=2$, in view of the secondary importance of this parameter to stability. Figure 3 shows growth rates against k for an unstable flow with different elastic wave speeds (but with $\alpha/\beta=2$), and displays an instability with long-wave character. As elastic wave speed decreases, the band of unstable wavenumbers widens, and by $\beta=2$, the unstable band extends to rather higher wavenumber.

Figure 4 shows further details of the growth rates for low and high wavenumber, and compares the numerical results with the asymptotic predictions derived above and

https://doi.org/10.1017/S0022112004002800 Published online by Cambridge University Press

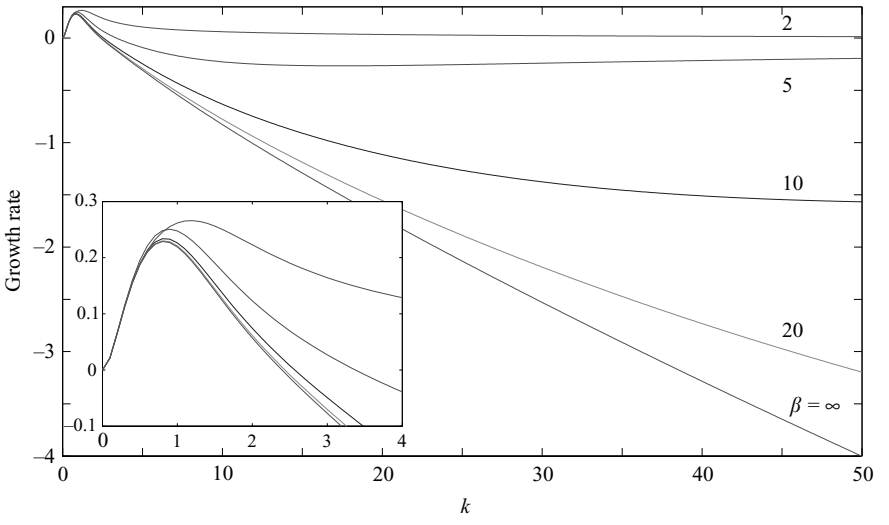


FIGURE 3. Sample growth rates against k for $R=2$ and $G=2$, and for a variety of elastic wave speeds with $\alpha/\beta=2$ and β as indicated.

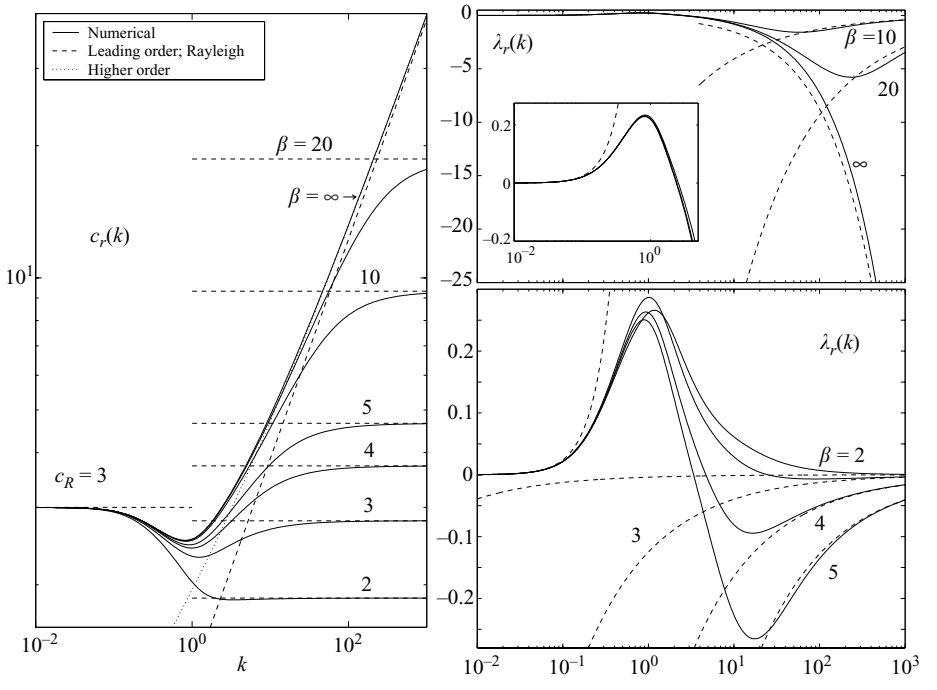


FIGURE 4. Wave speeds and growth rates against k for $R=2$ and $G=2$, and for a variety of elastic wave speeds with $\alpha/\beta=2$ and β as indicated. The numerical results are compared with the asymptotic predictions for long and short waves, as given in Appendix A (for the $\beta\to\infty$ wave speed, a higher-order approximation than given in the Appendix is also included; the slight improvement did not merit the inclusion of the actual formulae).

in the Appendix. In particular, this figure highlights the switch over from long waves, with $c_r=3$ and $\Lambda_r\sim(6R/5)k^2$, to short Rayleigh-like waves with weak damping rates (except for the curve with $\beta\to\infty$).

https://doi.org/10.1017/S0022112004002800 Published online by Cambridge University Press

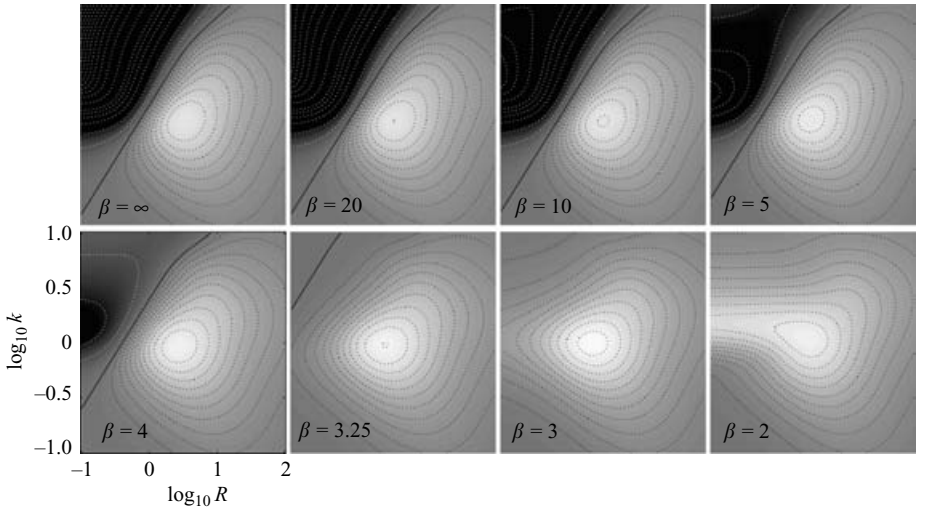


FIGURE 5. Growth rate shown as a density on the $(\log_{10} R, \log_{10} k)$-plane for the boundary-layer model with $\beta/\alpha = 2$ and $G = 2$. The dark dotted contours show positive growth rates and are separated by increments of 0.025. The light dotted contours show negative growth rates spaced by 0.25 from 0 to -1, and then in intervals of unity for smaller values. The solid contour displays the stability boundary.

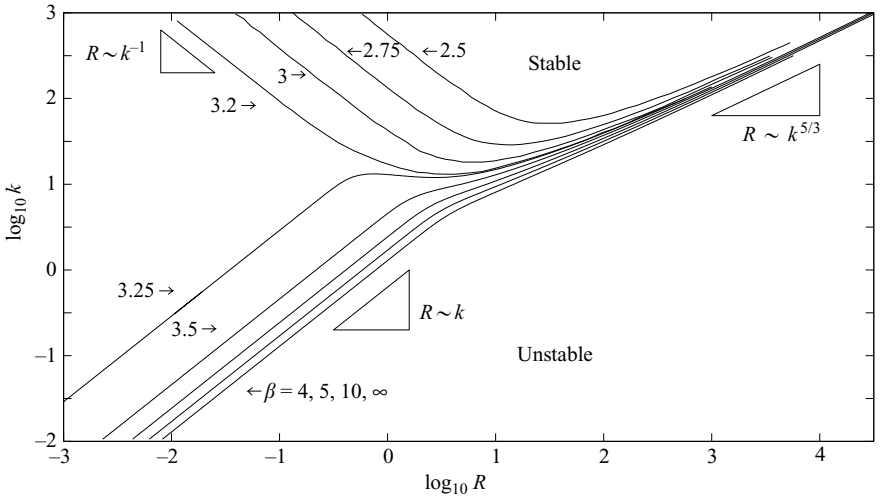


FIGURE 6. Stability boundaries on the $(\log_{10} R, \log_{10} k)$-plane for the boundary-layer model with $\beta/\alpha = 2$ and $G = 2$. The different curves correspond to different values of β. The dotted lines show the long- and short-wave limits of the stability boundary for $\beta \to \infty$.

We present more stability results in figures 5 and 6, which illustrate the effect of varying the elastic wave speed β for fixed $\alpha/\beta = 2$. Figure 5 shows a sequence of growth rates plotted as densities on the $(\log_{10} R, \log_{10} k)$-plane. The growth rates are largest for order-one wavenumber and R, irrespective of α/β. Stability boundaries are shown in figure 6. As the elastic wave speed is decreased, the range of unstable wavenumbers increases, and for $\beta < 3.22$, the stability boundary abruptly turns upwards to leave long waves unstable for $R \to 0$. The abrupt change in the stability boundary occurs for a Rayleigh wave speed of 3, and corresponds to the switch in sign of the elastic term in (4.6), as shown graphically in figure 2.

https://doi.org/10.1017/S0022112004002800 Published online by Cambridge University Press

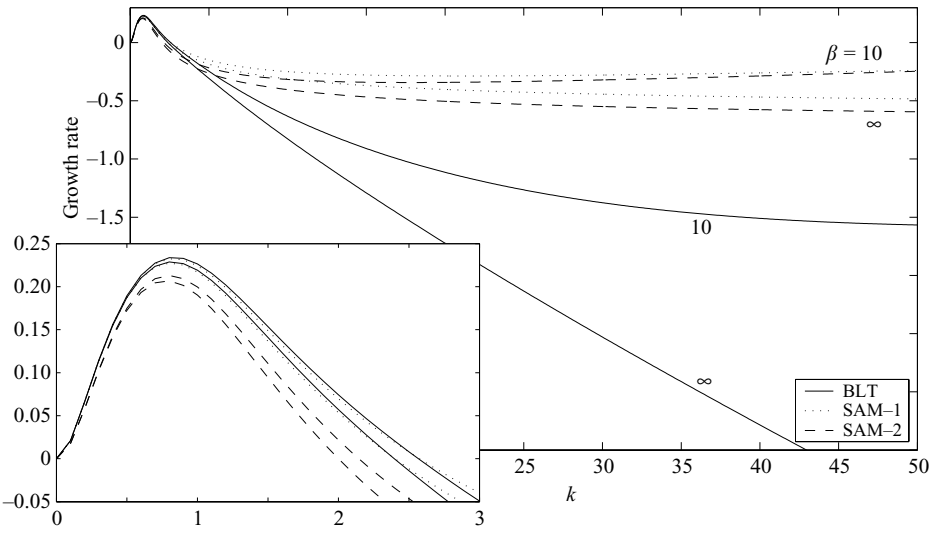


FIGURE 7. A comparison between the results of the boundary-layer theory (BLT) and the slot-averaged models (SAM). Shown are growth rates against k for $R=2$, $G=2$, $\alpha/\beta=2$ and $\beta=10$ and ∞.

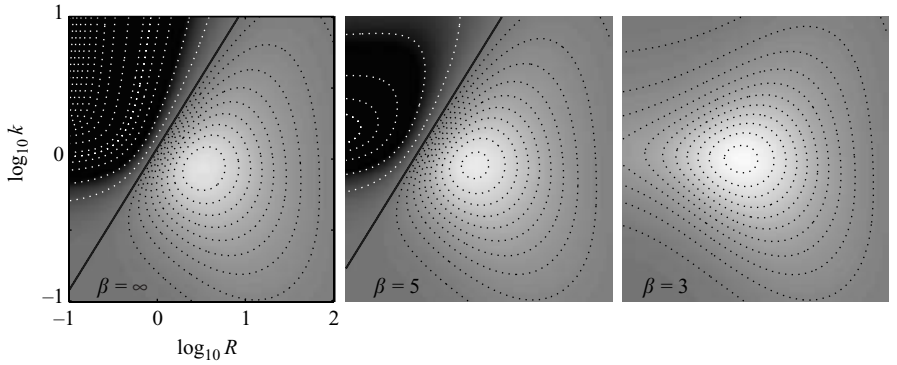


FIGURE 8. Growth rates shown as density on the $(\log_{10} R, \log_{10} k)$-plane for the improved slot-averaged model (3.12) with $\alpha=2\beta$, $G=2$ and $\beta=\infty$, 5 and 3. The contours have the same levels as in figure 5.

For large R, the stability boundary has the dependence, $R\sim k^{17/11}$, whereas at smaller R, we find either $R\sim k$ or $R\sim k^{-1}$, depending on whether β is above or below 3.22, respectively. The curious dependence, $R\sim k^{17/11}$, can be verified from short-wave theory along the lines sketched out above, but also adding the next term in the solution for ψ_I. This turns out to be necessary since $c\to 3/2$ on this part of the boundary, indicating that the neutrally stable inviscid solution ($|\varsigma|\to\infty$) can develop singularities along the midline of the conduit (where the wave speed matches the maximum flowspeed, i.e. the inviscid solution develops a critical layer). The third (short-wave, low β) part of the stability boundary, $R\sim k^{-1}$, corresponds to neutral Rayleigh waves with $c\to c_R$, for which there is no pressure perturbation at the wall, only a displacement (and kR arises as the eigenvalue of (4.2)).

Figure 7 displays a comparison between the results of the boundary-layer model and the two slot-averaged models presented earlier. Both averaged theories capture the long-wave instability, although the improved model compares better with the boundary-layer theory, as shown further in figure 8, which should be compared

https://doi.org/10.1017/S0022112004002800 Published online by Cambridge University Press

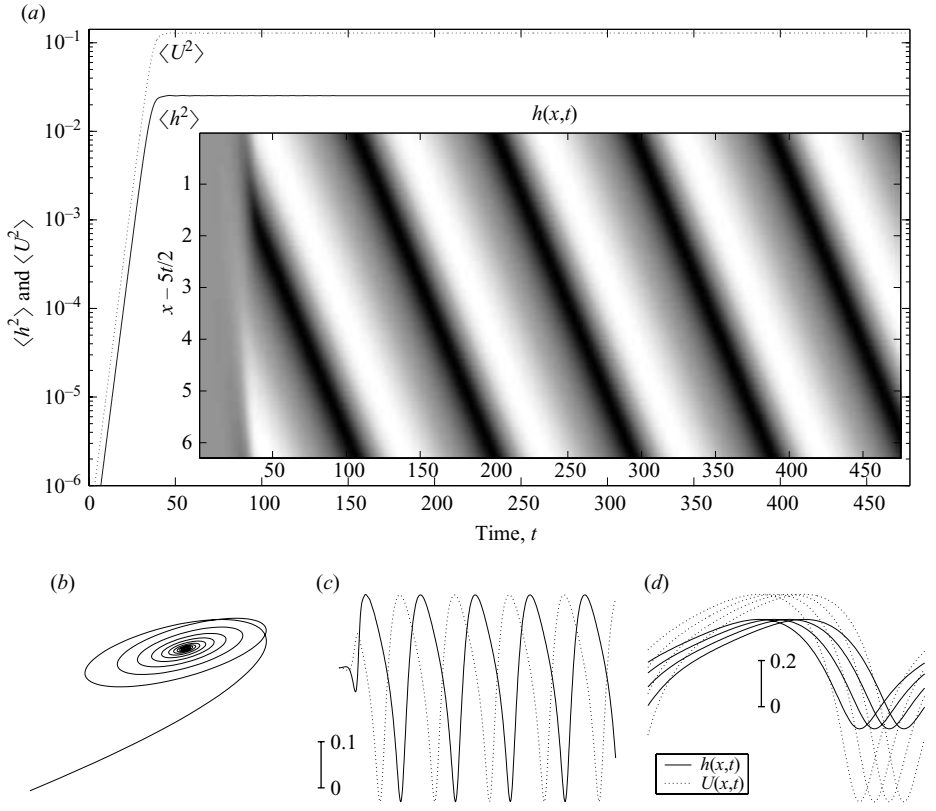


FIGURE 9. A numerical solution of the slot-averaged model (3.12) for $R = 1.5$, $\beta/\alpha = 1/2$ (with $\beta \to \infty$) and $G = 2$. (*a*) The averages of (5.2). The inset shows $h(x, t)$ as a density on the (t, x)-plane. (*b*)–(*d*) show further details of the solution. (*b*) A phase portrait on the $(\langle h^2\rangle, \langle U^2\rangle)$-plane. (*c*) Time series at two fixed positions. (*d*) Four snapshots of the solutions near the end of the computation.

with the relevant panels of figure 5. The comparison is less favourable at higher wavenumbers, where the growth rates are predicted to flatten out for the averaged theories whereas the actual damping rates of the boundary-layer model are stronger. Note that boundary-layer theory is strictly valid for small ϵk, and the high wavenumbers computed in the figures do not necessarily conform to this condition. The computations might then best be thought of as a test of the slot-averaged theories, which are essentially approximations of the boundary-layer model.

5. Nonlinear waves

To catch a glimpse of the nonlinear dynamics of unstable propagating waves, we solve the improved slot-averaged model (3.12) numerically in a periodic domain of length 2π. We adopt the simplifying assumption $(\omega/k) \ll \alpha, \beta$, and use a Fourier transform to compute the pressure in terms of the displacement of the wall:

$$h = 1 + \sum_{n=-\infty}^{\infty} h_n \, \mathrm{e}^{\mathrm{i}nx}, \qquad p = 2\mathrm{i}G(1 - \beta^2\alpha^2) \sum_{n=-\infty}^{\infty} n^2 h_n \, \mathrm{e}^{\mathrm{i}nx} \, \mathrm{sgn}(n). \tag{5.1}$$

The PDEs are then solved using a standard implicit time integrator after dealing with spatial derivatives with either a finite-difference or a pseudo-spectral scheme. Initial

https://doi.org/10.1017/S0022112004002800 Published online by Cambridge University Press

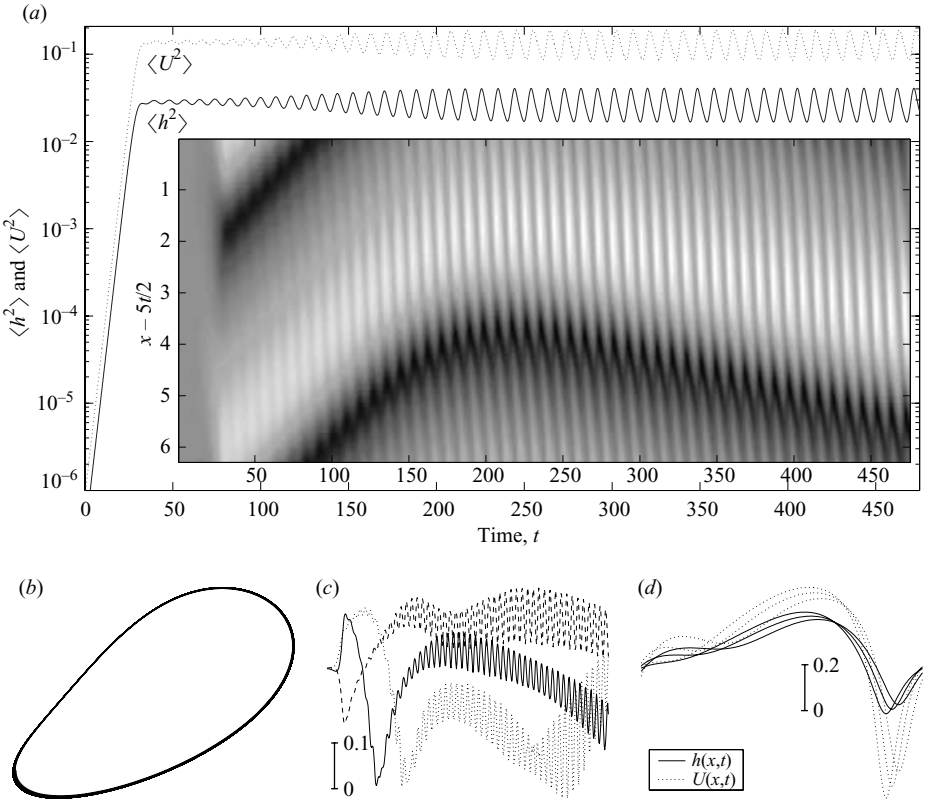


FIGURE 10. A similar set of pictures to figure 9, but for $R = 1.75$. (In this case, (*b*) the phase portrait shows only the final attractor, not the initial transient, (*c*) shows time series at three positions and (*d*) shows three profiles.)

conditions take the form of small random perturbations about the equilibrium state. The end result is the evolution of $h(x,t)$ and $q(x,t)$. For purposes of presentation, we define an average velocity, $U(x,t) = q/h$.

We first set $G = 2$ and show a suite of computations of increasing R (figures 9–11). The initial perturbations seed the growth of unstable waves, which ultimately saturate at finite amplitude. The wavelength of the fastest growing disturbance is given by linear theory, which is the longest wave in the box (i.e. $n = 1$ in (5.1)) if $G = 2$. For $R = 1.5$ (figure 9), the instability saturates in a steadily propagating wave. At fixed position, the time series of the wave takes the form of a periodic nonlinear oscillation, but in terms of the averages,

$$\langle h^2 \rangle = \int_0^{2\pi} h^2 \, \mathrm{d}x, \qquad \langle U^2 \rangle = \int_0^{2\pi} U^2 \, \mathrm{d}x, \tag{5.2}$$

the saturated wave is perfectly steady. As we gradually reduce the Reynolds number from 1.5 to the critical value at the threshold of instability, the level of saturation smoothly decreases to zero, in the usual manner of a supercritical bifurcation.

Somewhat above $R = 1.5$, the saturated nonlinear wave no longer remains steady. Near $R = 1.65$, the steady solution appears to lose stability to a second wave propagating with different speed. The result is a two-frequency pattern (a torus in phase space), which appears as a limit cycle in the averages of (5.2), as illustrated in figure 10 for $R = 1.75$. The solutions develop in a complicated fashion as we raise

https://doi.org/10.1017/S0022112004002800 Published online by Cambridge University Press

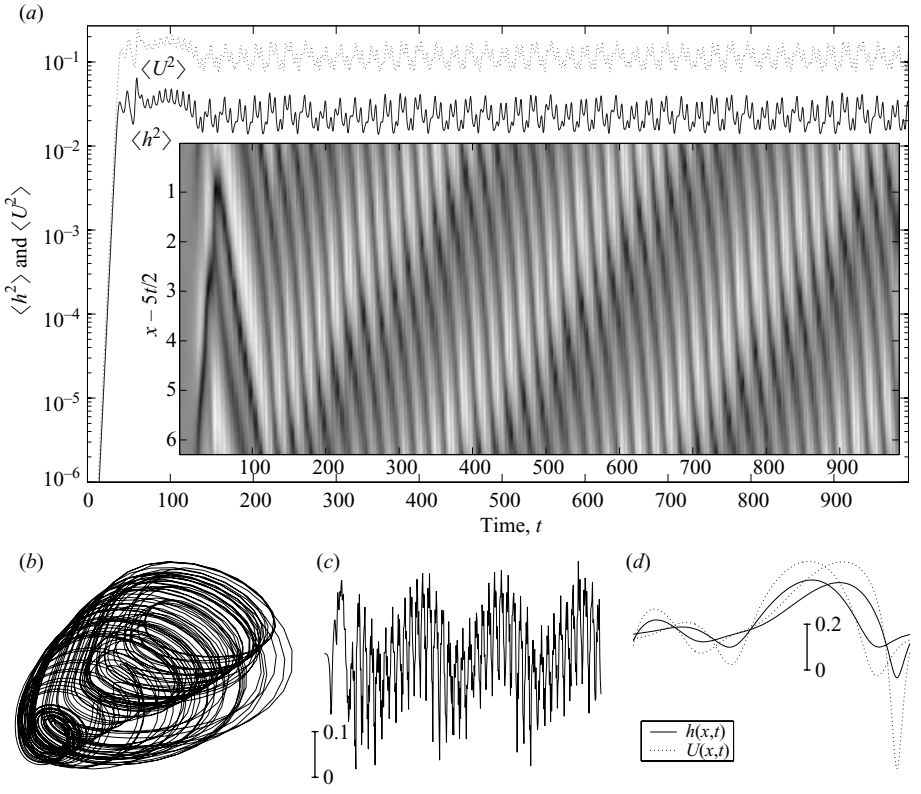


FIGURE 11. A similar set of pictures to figure 9, but for $R = 2.4$. (In this case, (*b*) the phase portrait shows only the final attractor, not the initial transient, (*c*) shows a time series at a single location and (*d*) shows two profiles.)

R still further; more bifurcations take place and there appears to be a transition to chaos, although we have not traced the precise pathway. Figure 11 shows what we interpret to be a chaotic solution at $R = 2.4$.

The waves connected to the solutions shown in figures 9–11 are not the only possible outcomes of the initial-value problem. Occasionally, other solutions appear abruptly on changing R, some of which are again steady. The new solutions have multiple peaks within each spatial period. Also, unsteady solutions with temporal oscillations in the averages of (5.2) can exhibit period-doubling phenomena on varying R. Thus, the system shows much scope for generating the nonlinear dynamics interpreted by Julian (1994, 2000) to underlie long-term variations of tremor frequency spectra.

One unsatisfying aspect of our computations at larger Reynolds numbers was that the 'improved' slot-averaged model began to display a tendency to jump from a regular solution to what appeared to be a singular solution that diverged in finite time. This behaviour is a known feature of thin-film equations (Ruyer-Quil & Manneville 2000) and signifies that the model is inadequate for larger values of R. By contrast, the simpler slot-averaged model shows no such singular features and generates solutions that remain regular at large R. To avoid the singular solutions we switched to the first slot-averaged model at larger Reynolds number. Aside from this difference, the solutions from both models at lower R were in qualitative agreement, although in the first model the bifurcations in behaviour occurred at slightly higher values of R.

https://doi.org/10.1017/S0022112004002800 Published online by Cambridge University Press

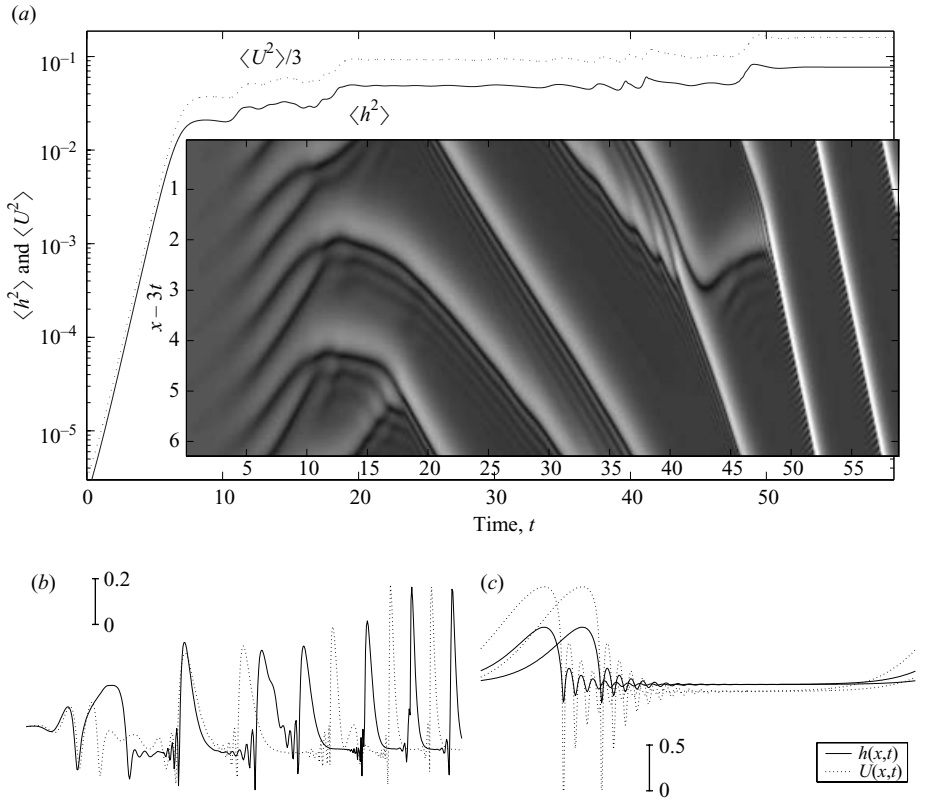


FIGURE 12. A simulation using the slot-averaged model (3.10) with $R = 0.3$ and $G = 0.1$ ($\alpha = 2\beta$ and $\beta \to \infty$). (*a*) The time history of the averages in (5.2) and $h(x, t)$ as a density on the (t, x)-plane. (*b*) Two time series at fixed position. (*c*) The final two snapshots of the wave profile.

Finally, we close this section by considering briefly what happens on varying G. The main effect of this parameter in linear theory is to rescale the wavenumber and R. In particular, when we reduce G, the maximum growth rates shift to higher wavenumber and the longest wave is no longer the most dominant. Instead, higher wavenumbers are expected to grow more quickly, suggesting that wave interactions could be important near onset. We show a sample solution in figure 12 which illustrates one of the more common types of behaviour. When wavetrains containing more than a single peak are initiated in the domain, an adjustment phase occurs beyond the initial saturation wherein waves attract one another and collide to form larger waves and 'coarsen' the spatial pattern. In figure 12, this process continues until only a single steadily propagating wave remains in the domain. Coarsening dynamics indicate that the most unstable wave predicted by linear theory is not necessarily the disturbance that is observed at finite amplitude. Instead, the character of tremor may be given by the length of the conduit.

6. Discussion

6.1. *Volcanic tremor*

Tremor accompanies nearly all volcanic eruptions and is a common eruption precursor (Konstantinou & Schlindwein 2002). However, the characteristics of tremor can vary

https://doi.org/10.1017/S0022112004002800 Published online by Cambridge University Press

considerably. The signal may originate from as deep as 40 km below ground level, or as shallow as a few hundred metres (Aki & Koyanagi 1981). It can have a gradual or abrupt onset, be harmonic or anharmonic, and last minutes, days or months (Konstantinou & Schlindwein 2002). Typically, the signal comes from less than 10 km depth, and the frequency spectra display a distribution of sharp peaks concentrated between 0.1–7 Hz. There can be systematic changes in tremor during eruptions including what appear to be period doublings and halvings.

Given the range of tremor properties, depths of origin and association with all styles of eruptions (explosive, effusive; magmatic, phreatic; passive degassing), there may be multiple origins of volcanic tremor. Several mechanisms for tremor generation have been proposed including bubble growth or collapse, jerky crack propagation, oscillations of magma chambers, resonance of fluid-filled cracks and flow-induced oscillations of conduits (Julian 1994; Konstantinou & Schlindwein 2002). Models involving resonance require a disturbance to trigger oscillations and while there are many plausible sources of so-called 'long-period' events, which decay after seconds or tens of seconds, tremor requires a disturbance that is sustained for minutes or even months. Sustained resonance could be caused by continued formation of shock waves (Morrissey & Chouet 2001) or gas slugs (Cruz & Chouet 1997; James *et al.* 2004), however, these seem to require special circumstances and do not explain tremor during volcanic eruptions of all styles and compositions. By contrast, flow-induced oscillations in the conduit walls could provide a source of sustained seismicity, lasting as long as flow continued at a sufficient speed. Moreover, although the sample results presented by Julian involve very high fluid velocities (45–110 m s^{-1}) and frequencies at the high end of tremor ($\sim$5 Hz), his model can explain the apparent nonlinear phenomena observed at several volcanoes (Julian 2000; Konstantinou 2002).

The theory we have presented amplifies further on Julian's mechanism: a linear stability analysis indicates that flow-induced oscillations can appear at arbitrarily low (but non-zero) Reynolds numbers. Furthermore, the stability of the system depends on the crack aspect ratio, fluid speed and elastic wave speeds. However, up to this point we have not considered the physical parameters relevant to volcanic tremor. To this end, we return to dimensional units (restoring the tildes to decorate dimensionless variables) and record the dimensionless critical wavenumber, $\tilde{k}_{cr}$, below which the system is unstable to long waves. From (4.7), with $\tilde{k} \sim 1$ (which corresponds to waves of wavelength comparable to the length of the crack), we find

$$1 \sim \frac{R}{G} = \frac{\rho U^2}{\rho_s \epsilon \beta^2} \qquad \text{or} \quad U \sim \left(\frac{\epsilon \rho_s}{\rho}\right)^{1/2} \beta, \tag{6.1}$$

where β is the true dimensional shear wave speed. Evidently, stability does not depend directly on viscosity, but the more viscous the fluid, the greater the pressure gradient required to drive flow at a given velocity through a crack with a given thickness.

The estimate in (6.1) is actually quite natural for our conduit, and can be arrived at more directly with dimensional analysis. The destabilizing inertial terms, $\rho(u_t + uu_x)$, are order $\rho U^2/L$. These are opposed by the pressure gradient, $p_x \sim p/L$, arising from the elastic stresses due to the deformation of the wall. Since the elastic displacements are order H, we see immediately from the constitutive relation that $p \sim \mu H/L$. The balance of pressure gradient and inertia then gives (6.1).

To assess the feasibility of our model for generating volcanic tremor we consider $\epsilon = 10^{-4}$ and $\beta = 2$ km s^{-1}, which are towards the low end of physically possible parameters. The estimate in (6.1) then suggests that flow speeds of tens of metres per second are required for instability. Figure 13 shows a more refined calculation

https://doi.org/10.1017/S0022112004002800 Published online by Cambridge University Press

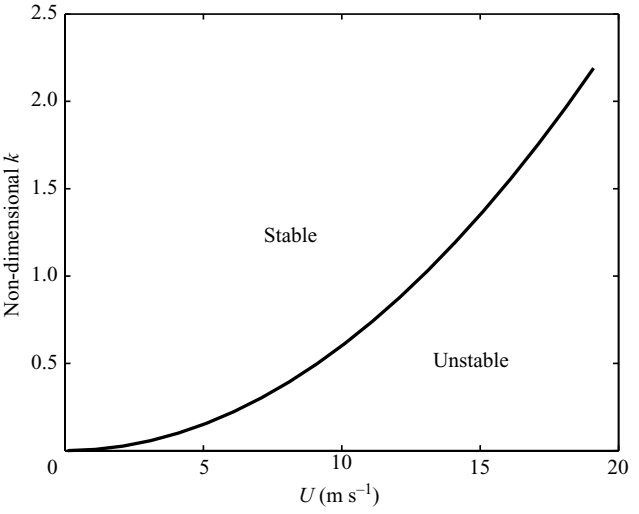


FIGURE 13. The curve on this plot of non-dimensional wavenumber versus average fluid velocity represents neutral stability for flow through a crack with aspect ratio $\epsilon = 10^{-4}$ in a solid with elastic wave speeds $\alpha = 4\,\mathrm{km\,s^{-1}}$ and $\beta = 2\,\mathrm{km\,s^{-1}}$, computed according to (4.7) with $\rho = \rho_s$.

based on the full expression of (4.7). However, even this figure indicates that with these relatively low ϵ and β values, average fluid velocities of $13\,\mathrm{m\,s^{-1}}$ or more are still required to induce oscillations. It might be possible for ϵ to be substantially less than 10^{-4}. However, even for $\epsilon = 10^{-6}$, as inferred by Cruz & Chouet (1997) for the source of long-period seismic events at Galeras Volcano (based on a crack resonance model), the critical average fluid velocity is still high.

The time scale associated with the instability is, in dimensional units, $L/3U$. Given the flow speed, tremor periods therefore constrain the length of the crack: for $U = 10\,\mathrm{m\,s^{-1}}$, the expected oscillation frequency is order one cycles per second when the crack length scale L is 10 m or so. In turn, this suggests a crack thickness (H) of millimetres if $\epsilon = 10^{-4}$ (which is required to reduce the critical flow speeds for instability). If tremor periods are as large as 10 s (e.g. Yamamoto *et al.* 2002) both the crack length and thickness can be made a factor of ten larger (hundreds of metres and centimetres, respectively). Thus, whilst the expected crack lengths are reasonable, and the nonlinear dynamics of unstable waves seems to be able to rationalize features of tremor spectra, the instability criterion remains far more constraining, and demands very narrow cracks and high fluid velocities.

6.2. *Aqueous and carbonaceous volcanic tremor?*

In other words, for Julian's mechanism to work, we require fluids to flow at speeds of order $10\,\mathrm{m\,s^{-1}}$ through narrow cracks beneath volcanoes, which seems excessive for subsurface flow of magma. Magma flow in the upper crust during explosive eruptions and fire-fountaining can reach hundreds of metres per second (Dobran 2001; Mangan & Cashman 1996). However, the viscosity of magma (10 to 10^{12} Pa s) makes sustained velocities of $10\,\mathrm{m\,s^{-1}}$ unreasonable for subsurface magma flow that is not coincident with, or immediately preceding, eruption at the surface. Therefore, it seems hard to generate flow-induced oscillations with magma.

The required condition for instability is more easily achieved for liquids such as groundwater or supercritical fluid exsolved from magma. These fluids have much

https://doi.org/10.1017/S0022112004002800 Published online by Cambridge University Press

lower viscosity than magma, allowing higher flow speeds, and do not have a large density contrast with rock (so ρ/ρ_s is not overly small). In fact, aqueous fluids are present at all volcanoes and eruptions of magma are typically preceded by increased gas emissions indicative of subsurface flow. Furthermore, if a low viscosity fluid is required for deep tremor, this could explain the general lack of long period seismicity in recharge zones beneath intermediate and silicic volcanoes where there is magma movement but the magma is not saturated in volatiles. However, this also begs the question of whether we could expect to find high-speed flow of aqueous fluid at the depths required to explain tremor.

To what depths are aqueous fluids present? There is growing evidence that magmas a few kilometers below volcanoes are often saturated in volatiles (mixtures of H_2O, CO_2, etc.; Wallace 2001), and consequently a free, low-viscosity fluid is expected at such levels. However, volatile solubility increases with depth, suggesting that there should be no free aqueous fluid below 10 km. Yet the deepest reported tremor originated about 40 km below Kilauea Volcano (Aki & Koyanagi 1980). Nevertheless, magmas can be saturated in volatiles at depths in excess of 10 km if there is sufficient CO_2 in the melt (e.g. Lowenstern 2001), and Gerlach *et al.* (2002) have calculated that a low viscosity fluid could exsolve about 30 km under Kilauea. Though still shallower than Aki & Koyanagi deepest tremor, this opens up the possibility that a carbonaceous fluid played a role in generating those deep sustained vibrations. In fact, substantial crystallization of stalled magma could lead to CO_2 saturation and fluid exsolution even at 40 km depth.

Volatile-rich fluids can also be generated at great depths by dehydration metamorphism of subducted oceanic crust. Tremor has recently been detected in the mantle at two subduction zones at depths where the down-going slab is expected to reach high enough temperatures for water release (Obara 2002; Rogers & Dragert 2003). The generation of tremor in the portion of the mantle where one would expect a separate water phase is consistent with a mechanism based on the flow of low viscosity fluids.

We conclude that although magma transport is unlikely to generate flow-induced oscillations, rapid flow of H_2O- or CO_2-rich fluids is a possible source for tremor (a) in the upper several kilometers of crust where aqueous fluids are present, (b) at greater depth where the magma has high CO_2 content, and (c) in the mantle above dehydrating subducted crust. Moreover, the same mechanism could produce 'long-period' events if the fluid only intermittingly achieves sufficient speed to induce wall oscillations. Note that a relatively dense fluid phase is essential, otherwise the density contrast with rock does not favour instability, which precludes a mechanism based on vapour flow.

6.3. *Conclusions*

Our stability analysis indicates that some fluids, conduit geometries and eruption styles are more likely to cause tremor by flow-induced oscillations than others. In particular, we have found that narrow conduits and high fluid speeds tend to generate flow-induced tremor. Also, as we argue in Appendix B, planar conduits seem far more unstable than tube-like fluid conduits. Except for shallow seismicity during explosive or fountaining activity, maintaining sufficient fluid speeds ($>10\,\mathrm{m\,s^{-1}}$) by realistic pressure gradients to induce oscillations requires sustained flow of low-viscosity aqueous or carbonaceous fluid rather than magma. These conclusions are consistent with observations by McNutt (2002) in a study of tremor from 50 eruptions at 31 volcanoes comparing tremor characteristics and corresponding eruption parameters.

https://doi.org/10.1017/S0022112004002800 Published online by Cambridge University Press

McNutt lists four trends in the data:

1) large eruptions produce stronger tremor than small ones;
2) fissure eruptions produce stronger tremor than circular vents for the same fountain height;
3) eruptions with higher gas content produce stronger tremor than those with low gas content at the same volcano; and
4) phreatic eruptions [*eruptions that eject broken rock and vapour but no magma*] produce stronger tremor than magmatic eruptions [*eruptions that do eject magma*] for the same VEI [*Volcanic Explosivity Index, a measure of the magnitude and intensity of an eruption*].'

Much remains to be done. First, and foremost, is to change the conduit geometry: an arguably more plausible configuration involves a relatively short conduit, bounded by fluid reservoirs at either end. In this latter case, flow instability arises when the walls rock back and forth in near unison, and the mathematical description invokes normal modes rather than waves. A key physical issue that must be addressed is whether the flushing action of the flow down the finite conduit can suppress instability (the periodic boundaries we have considered here allow waves to re-enter the conduit and continue to grow).

For the volcanic application, we must further develop the comparison with observations. The sole observations used here were the rough characteristics of tremor and the geological conditions. However, there are detailed seismic studies of tremor sources and decomposition of the outgoing elastic wavefield, both of which should be taken into consideration in testing the theoretical model. We note that the flow instability generates roughly equal amounts of shear-wave and compressional-wave radiation ($\chi \sim \phi$), and that the seismic signature may be similar to that already explored in acoustic resonance models for tremor (Chouet 2003, and references therein).

N. J. B. thanks Susan Schwartz for bringing this problem to his attention. This work began at the 2003 GFD Summer Study Program, Woods Hole Oceanographic Institution (which is supported by NSF and ONR). We thank the participants for discussions. We also thank two anonymous reviewers and K. Cashman and D. Villagomez for their comments. N. J. B. was supported by the National Science Foundation (Grant no. DMS 72521).

Appendix A. Short-wave results

In this Appendix, we present some of the details of the short-wave stability theory of the boundary-layer model. First, consider the limit $\beta \to \infty$, with α/β held fixed. Then, $D \sim 2k(1 - \beta^2/\alpha^2)$. Thus, considering $k \gg 1$, we find

$$c \sim \sqrt{\frac{2kG}{R}\left(1 - \frac{\beta^2}{\alpha^2}\right)}. \tag{A 1}$$

The first imaginary correction to c appears at order $k^{-1/4}$:

$$\mathrm{Im}(c) \sim -\frac{1}{2}\left[\frac{G(1 - \beta^2/\alpha^2)}{2kR^3}\right]^{1/4} \quad \text{or} \quad \mathrm{Re}(\Lambda) \sim -\frac{1}{2}\left[\frac{k^3 G(1 - \beta^2/\alpha^2)}{2R^3}\right]^{1/4}. \tag{A 2}$$

https://doi.org/10.1017/S0022112004002800 Published online by Cambridge University Press

Secondly, let β and α remain order one for $k \gg 1$. Then, if c remains order unity (specifically order β),

$$D(k, -\mathrm{i}kc) \to \frac{k\alpha\beta^2}{c^2\sqrt{\alpha^2-c^2}}\left[\frac{4}{\alpha\beta}\sqrt{(\alpha^2-c^2)(\beta^2-c^2)} - \left(2-\frac{c^2}{\beta^2}\right)^2\right] \equiv kD_R(c). \quad (A\,3)$$

The dispersion relation becomes

$$\frac{cR(3-c\varsigma)}{kG}\left\{1+\frac{(3-c\varsigma)}{(2c-3)}\left[1+\frac{2c}{\sqrt{3(2c-3)}}\tan^{-1}\sqrt{\frac{3}{2c-3}}\right]\right\}^{-1} = D_R(c), \quad (A\,4)$$

and so the leading-order eigenvalues correspond to zeros of $D_R(c_r)$, which gives the Rayleigh waves. The imaginary correction to the Rayleigh wave speed, c_R (which is of order β), appears at higher order. Provided $c_R > 3/2$, the growth rate follows from

$$\Lambda_r = \frac{(2c_R-3)^2}{GD_R'(c_R)}\sqrt{\frac{R}{2k|c_R|}}\left[1+\frac{2c_R}{\sqrt{3(2c_R-3)}}\tan^{-1}\sqrt{\frac{3}{(2c_R-3)}}\right]^{-2}. \quad (A\,5)$$

If α and β are relatively large (though not as large as k), the Rayleigh wave speed is also large, and we make further approximations to arrive at

$$Re(\Lambda) \sim \frac{|c_R|^{3/2}}{GD_R'(c_R)}\sqrt{\frac{R}{2k}}. \quad (A\,6)$$

If $\beta < 2$, the Rayleigh wave speed can become smaller than $3/2$ and a different scaling of growth rate then results. We ignore this possibility here.

Appendix B. The cylindrical conduit

Magma mostly rises through the Earth's brittle crust through fractures forming sheets of magma. Lava sometimes erupts from linear fissures. However, flow is usually localized by cooling, producing a cylindrical form at the top of the conduit. We now briefly assess the feasibility of flow through a cylindrical conduit generating tremor.

We consider a fluid-filled tube of length L and radius H in an elastic solid. The cylindrical coordinate system (r, θ, z) is set so that the z-axis is in the centre of the tube and the solid–fluid interface is at $r = h(z, t)$. Flow is two-dimensional with velocity field $(v, 0, w)$.

We non-dimensionalize as for the planar conduit, with x and y replaced with z and r, respectively. The non-dimensional boundary-layer equations are

$$R(w_t + ww_z + vw_r) = -p_z + \frac{1}{r}(rw_r)_r, \quad p_r = 0, \quad (B\,1)$$

and

$$w_z + \frac{1}{r}(rv)_r = 0. \quad (B\,2)$$

We content ourselves with a discussion of the linear problem using a slot-averaged approximation. We take the velocity of the fluid to be

$$w(r, z, t) = 2W(z, t)\left(1-\frac{r^2}{h^2}\right), \quad (B\,3)$$

https://doi.org/10.1017/S0022112004002800 Published online by Cambridge University Press

so that the tube-averaged velocity is $W(z,t)$ and the profile is parabolic. The radial integrals of (B 1) and (B 2) then lead to the system,

$$R(h^2W)_t + \tfrac{4}{3}R(h^2W^2)_z = -h^2p_z - 8W, \qquad (h^2)_t + (h^2W)_z = 0. \tag{B 4}$$

These equations support an equilibrium flow with $W=1$, $h=1$ and $p_z=-8$.

A short diversion into solving the elasticity equations in cylindrical geometry with a Fourier transform in z (with or without acceleration terms, and using the properties of Bessel functions) yields the leading-order matching condition,

$$p = \frac{2G}{\epsilon}[h(x,t)-1]. \tag{B 5}$$

(The dimensionless radial polar coordinates for the elastic solid must be taken to be (R,Θ,Z), with $R\in[\epsilon,\infty)$, and expansion for small ϵ eventually yields (B 5).)

Linear stability analysis about the equilibrium leads to the dispersion relation,

$$2\mathrm{i}kR\left(\frac{4}{3}+\frac{8\Lambda}{3\mathrm{i}k}-\frac{\Lambda^2}{k^2}\right)+16\left(2+\frac{\Lambda}{\mathrm{i}k}\right)=\frac{2\mathrm{i}kG}{\epsilon}, \tag{B 6}$$

and it is straightforward to show that waves are always stable.

A similar negative result can be obtained from a long-wave expansion of the boundary-layer model in (B 1)–(B 2). In that case, we can establish that, if the model is unstable, then the critical Reynolds number must be of order $G/\epsilon k$. This critical condition can be written in the alternative form, $U\sim\beta(\rho_s/\rho k)^{1/2}$ where β is the dimensional elastic shear wave speed. By contrast, the equivalent condition for the planar conduit is $U\sim\beta(\epsilon k\rho_s/\rho)^{1/2}$. Thus, for wavelengths of order of the crack length ($k=1$), the flow speed required for instability in the cylindrical conduit is much higher than in the planar conduit by a factor of order $\epsilon^{-1/2}$, and must exceed the elastic wave speeds.

These results are striking in view of known results for instability in flow through elastic tubes (i.e. the physiological problem; Pedley 1980), which occurs at finite Reynolds number. One difference is that physiological models often use empirical laws for the pressure and drag inside the tube. However, Kumaran's (1995) results also suggest that instability arises once flow speed exceeds a critical value, or if the elastic wave speed is reduced below a threshold, which is consistent with the results above if those critical elastic wave speeds are slower than the flow speed.

REFERENCES

Aki, K. & Koyanagi, R. 1981 Deep volcanic tremor and magma ascent mechanism under Kilauea, Hawaii. *J. Geophys. Res.* **86**, 7095–7109.

Balmforth, N. J. & Liu, J. 2004 Roll waves in mud. *J. Fluid Mech.* **519**, 33–54.

Balmforth, N. J. & Mandre, S. 2004 Dynamics of roll waves. *J. Fluid Mech.* **514**, 1–33.

Benjamin, T. B. 1960 Effects of a flexible boundary on hydrodynamic stability. *J. Fluid Mech.* **9**, 513–532.

Benjamin, T. B. 1963 The threefold classification for unstable disturbances in flexible surfaces bounding inviscid flows. *J. Fluid Mech.* **16**, 436–450.

Brook, B. S., Pedley, T. J. & Falle, S. A. 1999 Numerical solutions for unsteady gravity-driven flows in collapsible tubes: evolution and roll-wave instability of a steady state. *J. Fluid Mech.* **396**, 223–256.

Chang, H.-C. 1994 Wave evolution on a falling fluid film. *Annu. Rev. Fluid Mech.* **26**, 103–136.

Chang, H.-C., Demekhin, E. A. & Kopelevich, D. I. 1993 Nonlinear evolution of waves on a vertically falling film. *J. Fluid Mech.* **250**, 433–480.

Chouet, B. 2003 Volcano seismology. *Pure Appl. Geophys.* **160**, 739–788.

https://doi.org/10.1017/S0022112004002800 Published online by Cambridge University Press

Cruz, F. G. & Chouet, B. A. 1997 Long-period events, the most characteristic seismicity accompanying the emplacement and extrusion of a lava dome in Galeras Volcano, Colombia, in 1991. *J. Volcanol. Geotherm. Res.* **77**, 121–158.

Dobran, F. 2001 *Volcanic Processes: Mechanisms in Material Transport*. Kluwer.

Duncan, J. H., Waxman, A. M. & Tulin, M. P. 1985 The dynamics of waves at the interface between a viscoelastic coating and a fluid flow. *J. Fluid Mech.* **158**, 177–197.

England, A. H. 1971 *Complex Variable Methods in Elasticity*. Wiley-Interscience.

Gad-El-Hak, M., Blackwelder, R. F. & Riley, J. J. 1984 On the interaction of compliant coatings with boundary-layer flows. *J. Fluid Mech.* **140**, 257–280.

Gerlach, T. M., McGee, K. A., Elias, T., Sutton, A. J. & Doukas, M. P. 2002 Carbon dioxide emission rate of Kilauea Volcano: implications for primary magma and the summit reservoir. *J. Geophys. Res.* **107**, ECV3, 1–15.

Hagerty, M. T., Schwartz, S. Y., Garces, M. A. & Protti, M. 2000 Analysis of seismic and acoustic observations at Arenal volcano, Costa Rica, 1995–1997. *J. Volcanol. Geotherm. Res.* **101**, 27–65.

James, M. R., Lane, S. J., Chouet, B. & Gilbert, J. S. 2004 Pressure changes associated with the ascent and bursting of gas slugs in liquid-filled vertical and inclined conduits. *J. Volcanol. Geotherm. Res.* **129**, 61–82.

Julian, B. R. 1994 Volcanic tremor: nonlinear excitation by fluid flow. *J. Geophys. Res.* **99**, 11 859–11 877.

Julian, B. R. 2000 Period doubling and other nonlinear phenomena in volcanic earthquakes and tremor. *J. Volcanol. Geotherm. Res.* **101**, 19–26.

Konstantinou, K. I. 2002 Deterministic non-linear source processes of volcanic tremor signals accompanying the 1996 Vatnajökull eruption, central Iceland. *Geophys. J. Intl* **148**, 663–675.

Konstantinou, K. I. & Schlindwein, V. 2002 Nature, wavefield properties and source mechanism of volcanic tremor: a review. *J. Volcanol. Geotherm. Res.* **119**, 161–187.

Kumaran, V. 1995 Stability of the viscous flow of a fluid through a flexible tube. *J. Fluid Mech.* **294**, 259–281.

Kumaran, V., Fredrickson, G. H. & Pincus, P. 1994 Flow induced instability of the interface between a fluid and a gel at low Reynolds number. *J. Phys. Paris II* **4**, 893–911.

Landahl, M. 1962 On the stability of a laminar incompressible boundary layer over a flexible surface. *J. Fluid Mech.* **13**, 607–632.

LaRose, P. G. & Grotberg, J. B. 1997 Flutter and long-wave instabilities in compliant channels conveying developing flows. *J. Fluid Mech.* **331**, 37–58.

Love, A. E. 1944 *Treatise on the Mathematical Theory of Elasticity*. 4th edn. Dover.

Lowenstern, J. B. 2001 Carbon dioxide in magmas and implications for hydrothermal systems. *Mineralium Deposita* **36**, 490–502.

McNutt, S. R. 2002 Volcanic tremor and its use in estimating eruption parameters. *EOS Trans. Am. Geophys. Un., Fall Meeting Suppl.* **83**, F1500–F1501.

Mangan, M. T. & Cashman, K. V. 1996 The structure of basaltic scoria and reticulite and inferences for vesiculation, foam formation, and fragmentation in lava fountains. *J. Volcanol. Geotherm. Res.* **73**, 1–18.

Moriarty, J. A. & Grotberg, J. B. 1999 Flow-induced instabilities of a serous–mucus bilayer. *J. Fluid Mech.* **397**, 1–32.

Morrissey, M. M. & Chouet, B. A. 2001 Trends in long-period seismicity related to magmatic fluid compositions. *J. Volcanol. Geotherm. Res.* **108**, 265–281.

Muralikrishnan, R. & Kumaran, V. 2002 Experimental study of the instability of the viscous flow past a flexible surface. *Phys. Fluids* **12**, 775–780.

Muskhelishvili, N. I. 1953 *Some Basic Problems of Elasticity*. Noordhoff.

Obara, K. 2002 Nonvolcanic deep tremor associated with subduction in southwest Japan. *Science* **296**, 1679–1681.

Pedley, T. J. 1980 *Fluid Mechanics of Large Blood Vessels*. Cambridge University Press.

Rogers, G. & Dragert, H. 2003 Episodic tremor and slip on the cascadia subduction zone; the chatter silent slip. *Science* **300**, 1942–1943.

Ruyer-Quil, C. & Manneville, P. 2000 Improved modelling of flows down inclined planes. *Eur. Phys. J.* B *Fluids* **15**, 357–369.

https://doi.org/10.1017/S0022112004002800 Published online by Cambridge University Press

Ryan, M. P. 1987 Neutral boyancy and the mechanical evolution of magmatic systems. In B. O. Mysen (ed.) Magmatic Processes: Physiochemical Principles. *Spec. Publ. Geochem. Soc.* **1**, 259–287.

Shankar, V. & Kumaran, V. 2002 Stability of wall modes in fluid flow past a flexible surface. *Phys. Fluids* **12**, 2324–2338.

Srivatsan, L. & Kumaran, V. 1997 Stability of the interface between a fluid and a gel. *J. Phys. Paris II* **7**, 947–963.

Wallace, P. J. 2001 Volcanic SO_2 emissions and the abundance and distribution of exsolved gas in magma bodies. *J. Volcanol. Geotherm. Res.* **108**, 85–106.

Yamamoto, M., Kawakatsu, H., Yomogida, K. & Koyama, J. 2002 Long-period (12 sec) volcanic tremor observed at Usu 2000 eruption; seismological detection of a deep magma plumbing system. *Geophys. Res. Lett.* **29**, art. 1329.

https://doi.org/10.1017/S0022112004002800 Published online by Cambridge University Press